Mirror-symmetric double-negative metamaterial resonator with polarization insensitivity and tunable sandwiched structure for multiband wireless communications

Zhonghang Ji [a,b], Wei Cao [a], Mandi Gao [a], Yunqing Liu [a,b,*], Wei Chu [a,b,**], Qiong Zhang [a,b]

[a] College of Electronic Information Engineering, Changchun University of Science and Technology, Changchun, Jilin, 130022, PR China
[b] Jilin Provincial Science and Technology Innovation Center of Intelligent Perception and Information Processing, Changchun, Jilin, 130022, PR China

ABSTRACT

This paper presents a novel Double-negative (DNG) metamaterial (MM) resonator with a mirror-symmetric configuration, designed to exhibit multiband resonances in the S, C, and X bands. The resonator is fabricated using advanced processing techniques on a Rogers 5880 substrate and features electrodeposited copper. It consists of four equal regions, each containing interconnected split-ring resonators that are connected through a cross-shaped structure to ensure mirror symmetry. The simulation results demonstrate six resonance points at frequencies of 2.45 GHz, 4.27 GHz, 6.86 GHz, 8.98 GHz, 10.69 GHz, and 11.65 GHz. These resonances are characterized by near-zero/negative permeability, negative permittivity, refractive index, and impedance. Furthermore, the cross-polarization effect of incident waves is investigated.

Additionally, the potential for tunability of resonance frequencies is explored through a sandwiched configuration of the MM resonator, achieved by modifying the cover of the resonating patch. Moreover, the equivalent circuit model of the proposed MM resonator is in good agreement with practical measurements, validating the simulation results. The new tuning method for MM resonators holds the promise for future sensing applications and wireless communications.

1. Introduction

Metamaterials have attracted significant interests in the radio frequency (RF) and near-infrared spectra due to their extraordinary properties, such as negative permittivity, negative permeability, and refractive index. These properties enable a variety of applications, including antenna gain enhancement [1–3], absorbers [4–6], imaging [7], superlensing [8], biomedical sensors [9], invisible cloaks [10], and wireless communications [11–16]. The periodic arrays of subwavelength meta-atoms in metamaterial-based artificial

structures provide the ability to control and manipulate the amplitude, phase, and polarization of electromagnetic waves. However, designing single- or double-negative metamaterial structures for all types of structures at a specific resonance frequency remains challenging. Moreover, the lack of tunability limits the flexibility of practical applications, as the operating frequency is fixed once the structures are fabricated. Thus, research into various metamaterial structures and frequency tuning techniques is essential for realizing multiband wireless communications [17–21].

Metamaterial-based devices have been widely developed since the late 20th century, when Pendry's group proposed the classic split ring resonator (SRR) based MM [22,23]. Various MM structures, including electric-LC (ELC) resonators [24], H-shapes, cross-shapes, and others [25,26], have since been demonstrated and designed for various applications. For example, Samir et al. reported an epsilon negative (ENG) metamaterial structure that is ideal for isolation in MIMO antenna designs, achieving a maximum Envelop Correlation Coefficient (ECC) of up to 0.0001 [27]. Additionally, tunable MM resonators have been introduced, such as the one consisting of four quartiles with interconnecting two split rings in each quartile, which can tune the resonance frequency by varying the length of perpendicular metal stubs [28]. Jianfeng's et al. presented a square split-ring cavity on a non-through metal-insulator-metal (MIM) waveguide that exhibits multimode fano resonances, achieved by varying the refractive index [29]. Furthermore, an all-dielectric toroidal MM structure with dual-fano resonances has been demonstrated by Tianyu et al. holding potential applications in terahertz and optical spectrums [30]. Mohammad's group developed a meander-lines-based MM structure on an FR4 substrate that can be tuned by implementing switches to the split gaps, with four resonance frequencies covering S, C, X, and Ku bands, although deviations in resonance frequency were observed due to the absence of complete symmetry [31]. Other types of metamaterial-based resonators have been presented, including cross-coupled [32] and tri-band [33] structures, for applications in microwave and wireless communications. Saif et al. demonstrated a swastika-shaped MM structure that exhibits polarization-independent properties with five resonance frequencies [34], and Zian et al. proposed a polarization-insensitive metamaterial-based absorber in terahertz with an average absorption up to 95.1 % within the broadband of 1.1 THz [18]. Additionally, a MEMS-based tunable metamaterial has been developed with polarization-independent characteristics, achieved by employing two electrostatic comb-drive actuators to achieve the tunability of dual-band resonances in terahertz spectrum [35]. In addition, tunable terahertz metamaterial absorbers have been discussed using the unique property of vanadium dioxide (VO2) [36,37]. Md. Moniruzzaman et al. presented a mirror symmetric metamaterial-based resonator with five resonances covering L, S, C, and X bands, with frequency tuning achieved by varying the dielectric substrates, although the shifting of resonance frequencies at higher bands is not following the trend observed at lower bands [38]. Additionally, Bellal et al. reported an enriched symmetric hexagonal split ring resonator metamaterial in Ref. [14], which is fabricated on a lossy FR-4 substrate that exhibits triple band negative permittivity characteristics for satellite and Wi-Fi applications. Some other groups have presented work on metamaterial absorbers, all of which have demonstrated excellent absorption rates and are suitable within the Wi-Fi band (2 GHz–5 GHz). The mentioned researches above elaborate the application of multi-band metamaterial structures in wireless communication, including Bluetooth, Wi-Fi, and 5G/6G. However, studies on tunable multi-band metamaterial structures are relatively lacking.

In this study, we present a polarization-insensitive and symmetric DNG metamaterial resonator and perform an analysis of its electromagnetic characteristics. We have successfully achieved six resonance frequencies covering the S, C, and X bands. The resonator-based MM can be subdivided into four meta-atoms, with each meta-atom being mirror-symmetric with its adjacent ones and center-symmetric with the diagonal one. This unique symmetric configuration effectively eliminates the coupling impact between the unit cells and minimizes the deviation of resonance frequency between the meta-atom and its arrays. Moreover, the proposed MM resonator exhibits exceptional properties of negative refractive index, negative permittivity and permeability. Additionally, a sandwiched MM resonator is constructed that demonstrates the tunability of resonance frequency by varying the gap opening of the dielectric layer atop the MM structure. This feature holds significant potential for various applications in microwave and wireless communications. To further verify the behavior of the proposed MM resonator, an equivalent circuit is designed in Advanced Design System (ADS), which matches the results obtained in CST Studio Suite 2022. Finally, experimental measurements were performed,
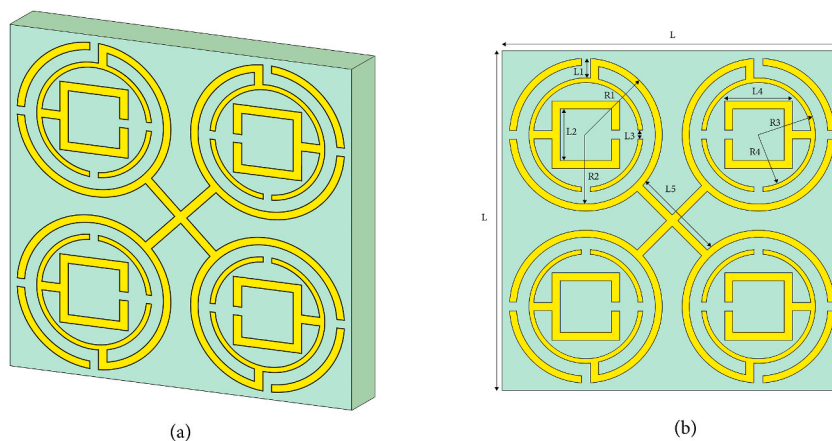

Fig. 1. (a)Proposed MM unit cell. (b)Configuration of labeled patch within the proposed MM structural arrangement.

which showed perfect good agreement with the numerical simulations.

2. Methodology of proposed MM structure

2.1. Introduction of metamaterial (MM) structure

The MM unit structure proposed in this paper is built on a Rogers substrate (RT5880) with dimensions of 20 × 20 × 1.575 mm, as shown in Fig. 1(a). The resonant patch is constructed on one side of the substrate material with a copper foil thickness of 0.035 mm. It is subdivided into four sub-element atoms, each of which has three interconnected split-ring resonators (SRRs), with the outer two being circular and the innermost one being square. The four sub-element atoms are connected by a cross-shaped structure as shown in Fig. 1 (b). This design helps to eliminate the coupling effect within the element atoms, thereby minimizing the resonance deviation between the element atoms and their arrays. In the simulation, the dimensions and separation gap of the rings and rectangles were adjusted and optimized to obtain the best response of the proposed MM structure. In Table 1, the optimized dimensions of different segments of the MM are included. The three-dimensional structural simulation arrangement is shown in Fig. 2, where the z-axis uses two waveguide ports, and the transverse electromagnetic (TEM) signal is vertically incident on the resonant patch from one waveguide port. The signal sent through the MM structure is received by another port. In the simulation arrangement, the x-axis adopts an electric boundary, the y-axis adopts a magnetic boundary, and the table contains the optimized size parameter values of the MM in the simulation of the frequency range from 1 to 12 GHz, and ultimately obtained the transmission coefficient (S21) and reflection coefficient (S11).

2.2. Evolutionary steps of the proposed MM unit cell

The design was mainly started on a 20 × 20 mm^2 substrate, and four resonant rings with two split gaps of each along the horizontal and vertical axes were placed in the form of a 2 × 2 array, as shown in Fig. 3 Design 1. This split-loop resonator provides a broadband resonance with the resonating frequency of 5.69 GHz, as shown in Fig. 4(a). Next, an additional split ring was added to the ring to form a mirror-symmetric structure, and one side of the split ring was connected to the outer ring, as shown in Fig. 3 Design 2. Due to the mutual inductance between the two rings, the inductive effect of the outer ring was changed, causing an early resonance shift at 8.99 GHz as shown in Fig. 4(a). The design then included a square ring inside the two circular rings, which had a split gap along the horizontal axis and was connected to the outer ring, as shown in Fig. 3 Design 3. These interconnected split-ring resonators provided three resonant frequencies at 6.74 GHz, 9.92 GHz, and 11.65 GHz. The additional split square ring had a significant impact on the resonant frequency and initial resonance bandwidth.

Furthermore, two cross-connected rectangular copper strips were added to the center of the 2 × 2 array to form a mirror-symmetric pattern, as shown in Fig. 3 Design 4. This helps to eliminate harmonic generation due to the coupling effect between unit cells during array formation. Finally, the transmission coefficient (S21) response of the MM structure produced resonances at 2.45 GHz, 4.27 GHz, 6.86 GHz, 8.98 GHz, 10.69 GHz, and 11.65 GHz, covering the S, C, and X bands, as shown in Fig. 4(a), whereas reflection coefficients (S11) plots of various design steps are presented in Fig. 4(b). Information related to S21 for various design steps is summarized in Table 2.

3. Analysis of numerical and experimental results

3.1. Equivalent circuit modeling of proposed MM structure

In order to have a better understanding on the proposed MM structure, the equivalent circuit model of the metamaterial (MM) is further investigated in this study by using ADS. The MM resonant configuration can be considered as a combination of different inductor(L)-capacitor(C) circuits shown in Fig. 5(a). Every split ring resonator represents an LC series circuit showing a certain resonance frequency (f $= \frac{1}{2\pi\sqrt{LC}}$), which can be tuned by varying dimension and gap of the ring resonator. In the LC equivalent circuit, the copper strip inductances in the outermost ring are represented by L1, L4, L17, and L10, and the capacitances produced by the split gap on the ring are represented by C1, C4, C7, and C10. The equivalent LC of the middle ring is represented by L2 and C2, L5 and C5, L8 and C8, and L11 and C11, while the inductances in the innermost ring are represented by L3, L6, L9, and L12, and the capacitances in series with the split ring are represented by C3, C6, C9, and C12. L13, L14, L15, and L16 are the inductances generated by the coupling of two cross-connected copper strips. All the LC values in the equivalent circuit model are provided in Tables S1 and S2 in the supplementary Information. Two ports are connected to the both sides of the equivalent circuit, serving as the transmitting and receiving ports, respectively, with an impedance termination of 50Ω. Later, the LC circuit is designed and simulated in ADS, and the result of

Table 1
Design parameters of proposed MM unit cell.

Parameter	Dimension(mm)	Parameter	Dimension(mm)	Parameter	Dimension(mm)
L	20	L1	1.14	L2	3
L3	0.5	L4	4	L5	5.5
R1	4.5	R2	4.06	R3	3.36
R4	3.06				
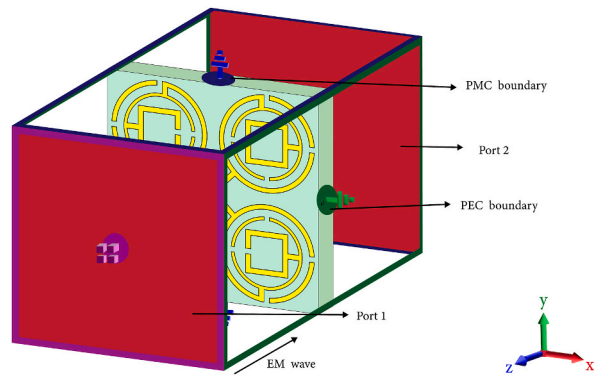
Fig. 2. Computational configuration of proposed MM unit cell (CST Studio Suite 2022).

Design 1   Design 2   Design 3   Proposed unit cell

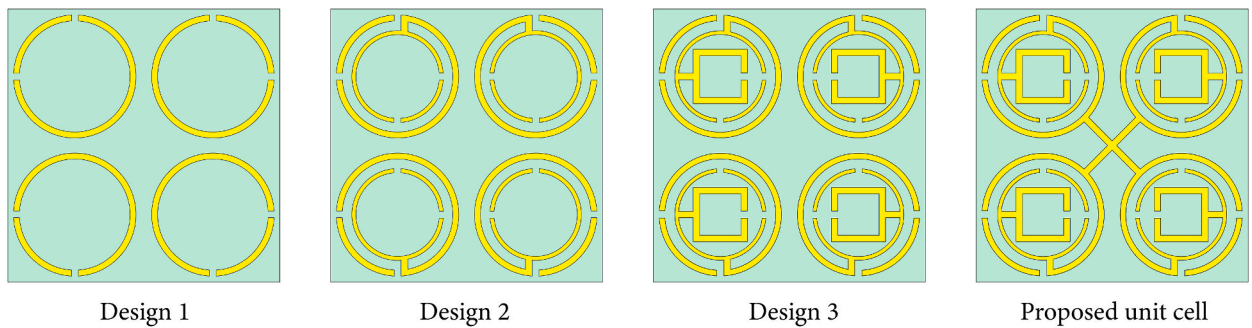**Fig. 3.** Sequential developmental stages leading to the envisioned unit cell (CST Studio Suite 2022).

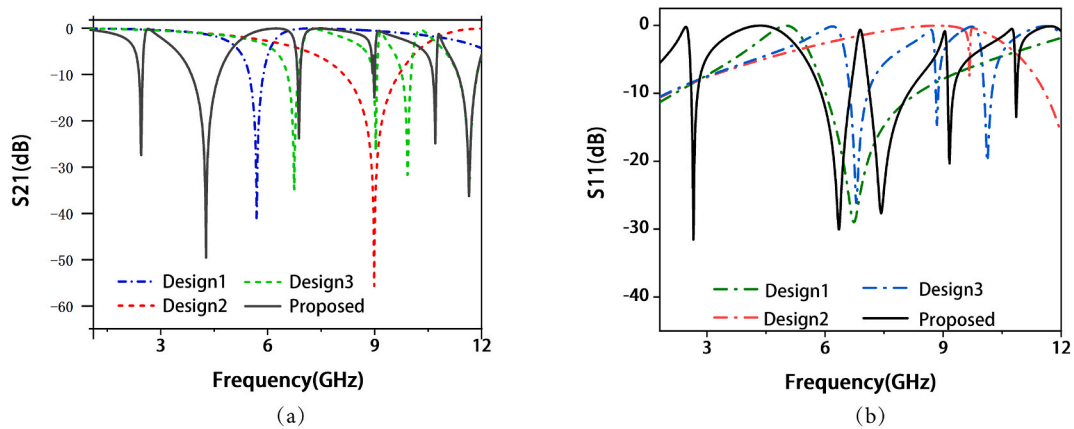(a)   (b)

Fig. 4. Scattering parameters of different stages in the development of the proposed unit cell: (a) Transmission coefficient (S21). (b) Reflection coefficient (S11).

Table 2
Performance evaluation of design steps in the development process of the proposed unit cell.

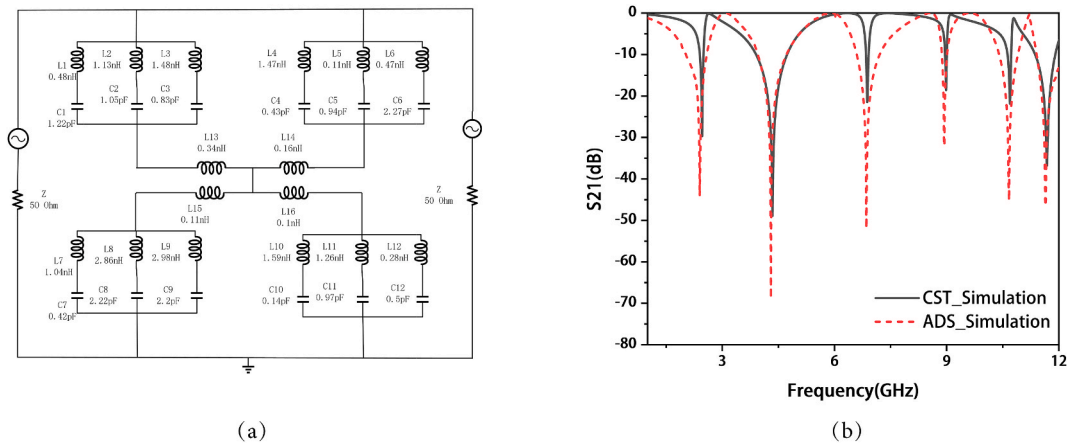| Substructure	Resonance frequency(GHz)	Bandwidth(GHz)	Resonance peak(dB)	Covering bands
Design 1	5.69	0.40	−41	C
Design 2	8.99	1.53	−55.67	X
Design 3	6.74, 9.92, 11.65	0.11, 0.26, 0.53	−34,-26,-31.69	C, X
Proposed unit cell	2.45, 4.27, 6.86, 8.98, 10.69, 11.65	0.10, 0.81, 0.10, 0.05, 0.11, 0.45	−27.4, −49.5, −23, −14.96, −24.9, −36.26	S, C, X

Fig. 5. (a) Equivalent circuit of the proposed unit cell, (b) Comparison of S21 response between circuit-level simulation in ADS and 3D structural simulation in CST.

transmission coefficient(S21) has a great agreement with that obtained from CST shown in Fig. 5(b).

3.2. Frequency tuning of the proposed MM structure

In metamaterials, electromagnetic interactions occur between the metamaterial and the incident waves. Due to the inductive characteristics of the copper strip and the capacitance generated by the gap between the metal rings, the entire structure can be considered as a resonant circuit. Thus, electromagnetic resonance occurs in metamaterials, and its frequency depends on the inductance and capacitance values contributed by the configuration of structure. When the dielectric material was placed on the MM structure, the effective permittivity of the entire structure is changed accordingly, resulting in the change of resonant frequencies. As the coverage area of the medium varies, the tunable resonant frequency is achieved.

Inspired by that, the Sandwiched metamaterial (SMM) structure is formed by adding a Rogers 5880 resonant patch atop the proposed MM structure, as shown in Fig. 6(a). The thickness of the added resonant patch is 1.575 mm. By varying the transverse gap widths (g) shows in Fig. 6(b), the frequency tuning can be observed. Fig. 7 shows the resonant frequency response varies at different gap widths, ranging from 1 mm to 5 mm with a step size of 1 mm in CST. Fig. 7(a) illustrates that the first resonant point gradually shifts towards higher frequencies as the gap width increases. Similarly, Fig. 7(b) and (c) also display the same trend, although the shift magnitude in Fig. 7(c) is relatively larger. Fig. 7(d) shows the variation of the last three resonant points at different widths, all of which exhibit an overall trend of shifting towards higher frequencies.
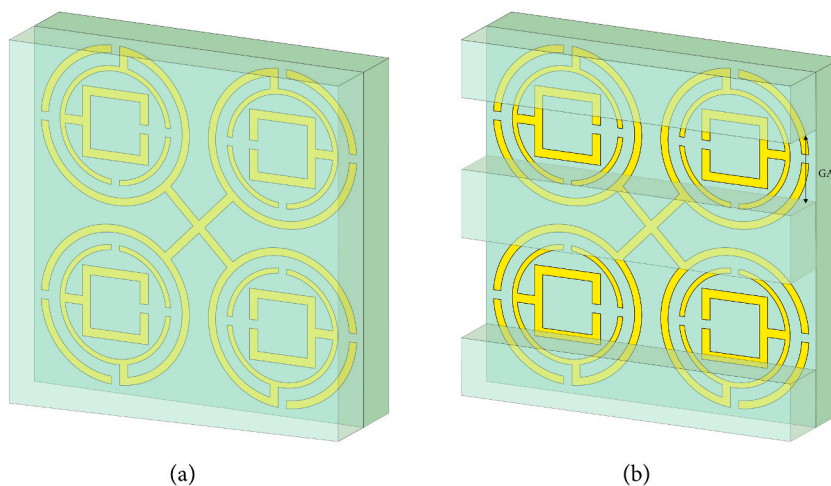

Fig. 6. Computational configuration for simulating the sandwiched metamaterial unit cell: (a) SMM configuration with Full coverage (b) SMM configuration with Gap opening.
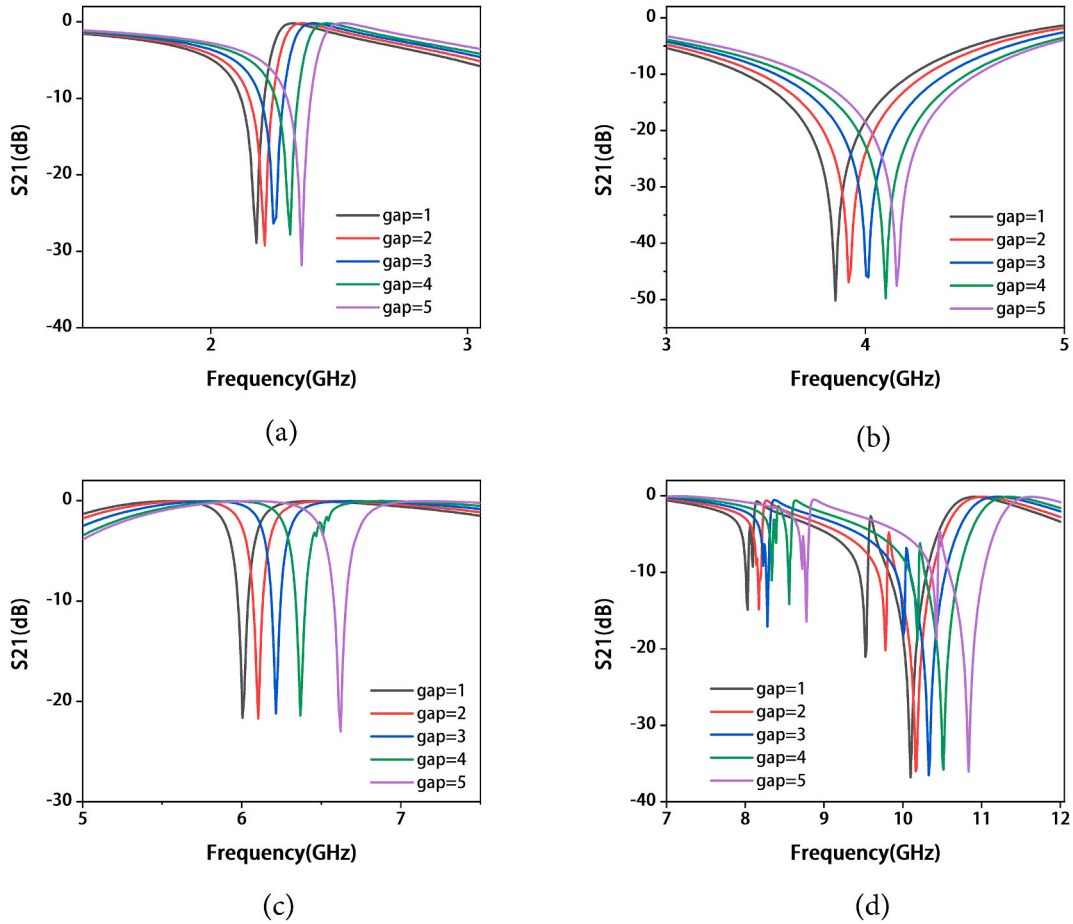
Fig. 7. S21 response of proposed MM structure with different values of gap: (a)1–3 GHz, (b)3–5 GHz, (c)5–8 GHz, (d)7–12 GHz.

3.3. Effective parameter analysis

The proposed metamaterial (MM) interacts with the incident electromagnetic wave, leading to resonance occurs in the reflected and transmitted signals. Fig. 8(a) illustrates the resonance pattern of these signals, specifically showing S21 resonances at frequencies of 2.45 GHz, 4.27 GHz, 6.86 GHz, 8.98 GHz, 10.69 GHz, and 11.65 GHz. The bandwidth of these resonances was obtained as 100 MHz, 810 MHz, 100 MHz, 50 MHz, 110 MHz, and 540 MHz, respectively. In addition, the reflection coefficient in Fig. 8(a) exhibits resonance at frequencies of 2.65 GHz, 6.36 GHz, 7.42 GHz, 9.16 GHz, and 10.85 GHz. The proposed MM demonstrates a broadband response in the transmitted signal within the frequency range of 3.93–4.74 GHz. Additionally, a wideband response is observed within the range of 11.41–11.95 GHz, covering the C and X bands. The other resonant bands are relatively narrow, collectively covering the S, C, and X bands.

The electromagnetic properties of the MM are analyzed by utilizing a CST post-processing template through the transmission (S21) and reflection (S11) coefficients. Later, these coefficients are employed by using a robust retrieval method [39] to calculate the permittivity, permeability, refractive index and normalized impedance of the MM. The retrieval method is specifically designed to handle the scattering parameters involved in the analysis. The transmission (S21) and reflection (S11) coefficients were realized by equations:

$$S_{11} = \frac{R_{01}(1 - e^{i2nk_0d})}{1 - R_{01}^2 e^{i2nk_0d}}, \tag{1}$$

$$S_{21} = \frac{(1 - R_{01}^2)e^{ink_0d}}{1 - R_{01}^2 e^{i2nk_0d}}, \tag{2}$$

where,
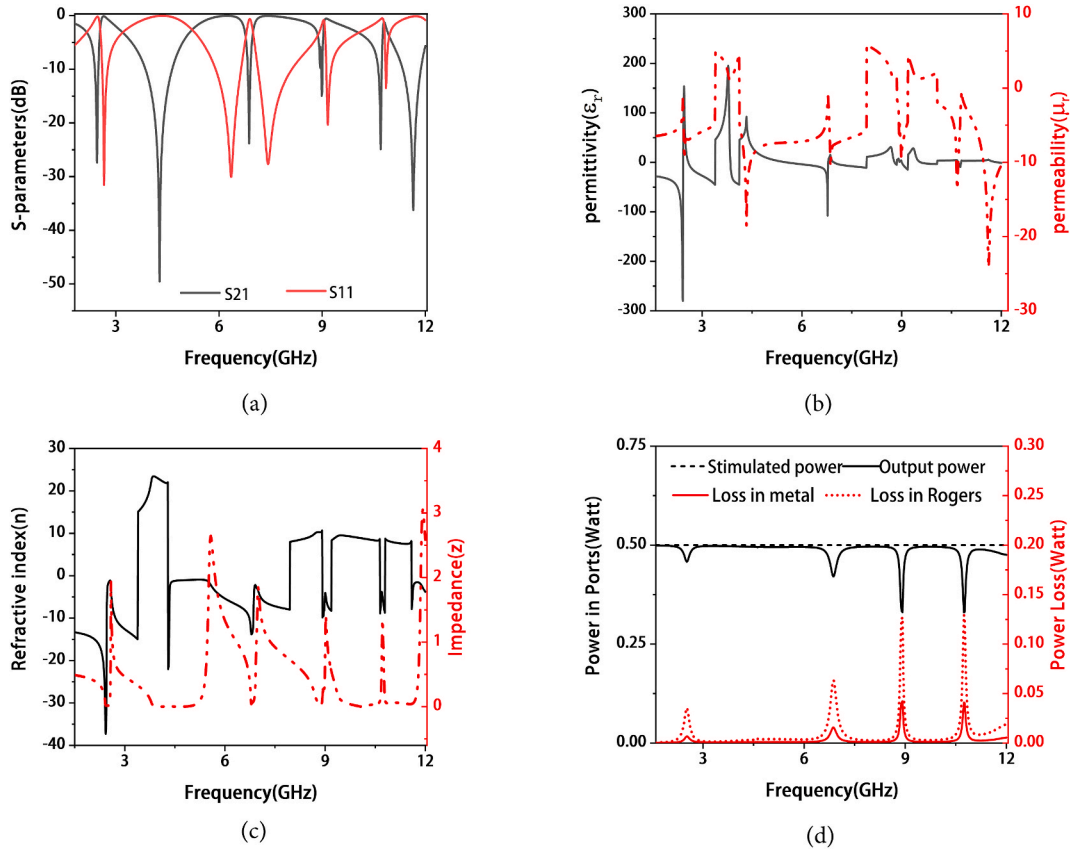
$$R_{01} = z - 1/z + 1, \tag{3}$$

Fig. 8. (a) Reflection(S11) and transmission(S21) coefficient plot (b) permittivity(ε_r) and permeability(μ_r) (c) refractive index(n) and impedance(z) (d) power conversion.

$$e^{ink_0 d} = \frac{S_{21}}{1 - S_{11}\frac{z-1}{z+1}} \tag{4}$$

The normalized impedance was calculated by using S11 and S21 as:

$$\text{Impedance}: z = \pm \sqrt{\frac{(1+S_{11})^2 - S_{21}^2}{(1-S_{11})^2 - S_{21}^2}} \tag{5}$$

$$\text{refractive index}, n = \frac{1}{k_0 d}\cos^{-1}\left[\frac{1}{2S_{21}}\left(1 - S_{11}^2 + S_{21}^2\right)\right] \tag{6}$$

$$= \frac{1}{k_0 d}\left\{\left[\ln\left(e^{i2nk_0 d}\right)'' + 2m\pi\right] - i\left[\ln\left(e^{i2nk_0 d}\right)'\right]\right\}$$

where $(\cdot)'$ is the real part, $(\cdot)''$ is the imaginary part, m is an integer related to the real part of the refractive index, k0 is the wave number of the incident wave in free space, and d is the thickness of the substrate. Permittivity and permeability can be calculated using the equations:

$$\text{permeability}, \mu = nz \tag{7}$$

$$\text{permittivity}, \varepsilon = n/z \tag{8}$$

The frequency response of relative permittivity and permeability at different frequencies are given in Fig. 8 (b). It can be seen from the figure that relative permittivity has negative values in the frequency range of 1–2.42 GHz, 2.58–3.39 GHz, 3.85–4.11 GHz, 5.53–6.79 GHz, 6.96–7.94 GHz, 8.79–8.85 GHz, 9.0–9.18 GHz, 9.58–10.06 GHz, 10.71–10.79 GHz, 11.89–12 GHz. On the other hand, the negative relative permeability is falling within the frequency range of 1–3.39 GHz, 4.12–7.94 GHz, 8.87–9.18 GHz, and 10.08–12 GHz. Therefore, the frequency bands with DNG characteristics (negative permittivity and negative permeability) were obtained in the frequency range of 1–2.42 GHz, 2.58–3.39 GHz, 5.53–6.78 GHz, 6.96–7.94 GHz, 9.0–9.18 GHz, 10.71–10.79 GHz, 11.89–12 GHz,

which is further verified by negative refractive index (n) shown in Fig. 8(c). The comparison of related simulated parameters and measured data is plotted in Fig. S1 in the Supplementary Information. In addition, the power associated with the proposed MM structure is investigated and shown in Fig. 8 (d). The total power at port 1 is 0.5 Watt and most of the power over the entire frequency band was received by port 2. There are four predominant dips observed at 2.5 GHz, 6.9 GHz, 9.0 GHz and 10.8 GHz in the curve of output power, which were caused by the loss of metal and dielectric.

Furthermore, systematic simulations were performed to investigate the impact between polarization and incident angle. Fig. 9 visually represents the results, demonstrating that the suggested structure possesses a remarkable insensitivity towards both polarization and incident angle. In Fig. 9(a), the response of the transmission coefficient S21 is depicted at different polarization angles, ranging from 0° to 90° with a step size of 15°. Similarly, Fig. 9(b) illustrates the effect of the incident angle on the transmission coefficient S21, setting the angle range that matches the polarization angle. It can be seen in Fig. 9 that the proposed structure remains unaffected by variations in polarization angle and incident angle, which holds the potential to be implemented in wireless communication applications from a scientific perspective.

3.4. Surface current, electric field, and magnetic field analysis

Maxwell's equations elucidate the intricate interconnection between the electric field (E-field), magnetic field (H-field), and surface current within a metamaterial. The surface current delineates the genuine current engendered by the incoming electromagnetic field. This authentic current engenders the magnetic field, and alterations in this magnetic field are pivotal for generating the electric potential. The e-field and h-field can be expressed by the following equation:

$$\nabla \times H = J + \frac{\partial D}{\partial t} \tag{9}$$

$$\nabla \times E = -\frac{\partial B}{\partial t} \tag{10}$$

where,

$$\nabla = \left[\frac{\partial}{\partial x}, \frac{\partial}{\partial y}, \frac{\partial}{\partial z} \right] \tag{11}$$

Therefore, the other two equations can also be employed to establish the relationship between electromagnetic fields and metamaterials.

$$D(t) = \varepsilon(t) * E(t) \tag{12}$$

$$B(t) = \mu(t) * H(t) \tag{13}$$

where E and H denote the time-varying E-field and H-field intensities, D and B denote the time-varying electric and magnetic flux densities, ε is the electric permittivity, μ is the magnetic permeability, and J represents the time-varying current density in the medium.

In order to further analyze the proposed structure, this paper systematically simulates and verifies the distribution characteristics of surface current, electric field, and magnetic field. Fig. 10 illustrates the distribution characteristics of surface current, electric field, and magnetic field at six different resonance frequencies. As can be seen from Fig. 10(a1) at 2.45 GHz, the strong circulating current is mainly concentrated on both sides of the y-axis. Although the current flows in opposite directions in the outermost rings of each unit,
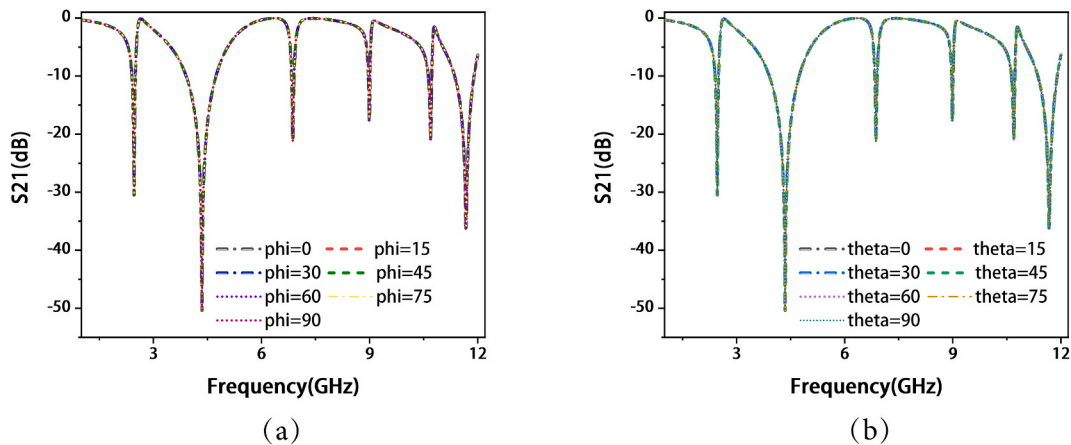

Fig. 9. The effect of incident waves with different polarizations in the S21 of proposed MM in CST simulation: (a) polarization (φ) variation (b) Incident angle(θ) variation.

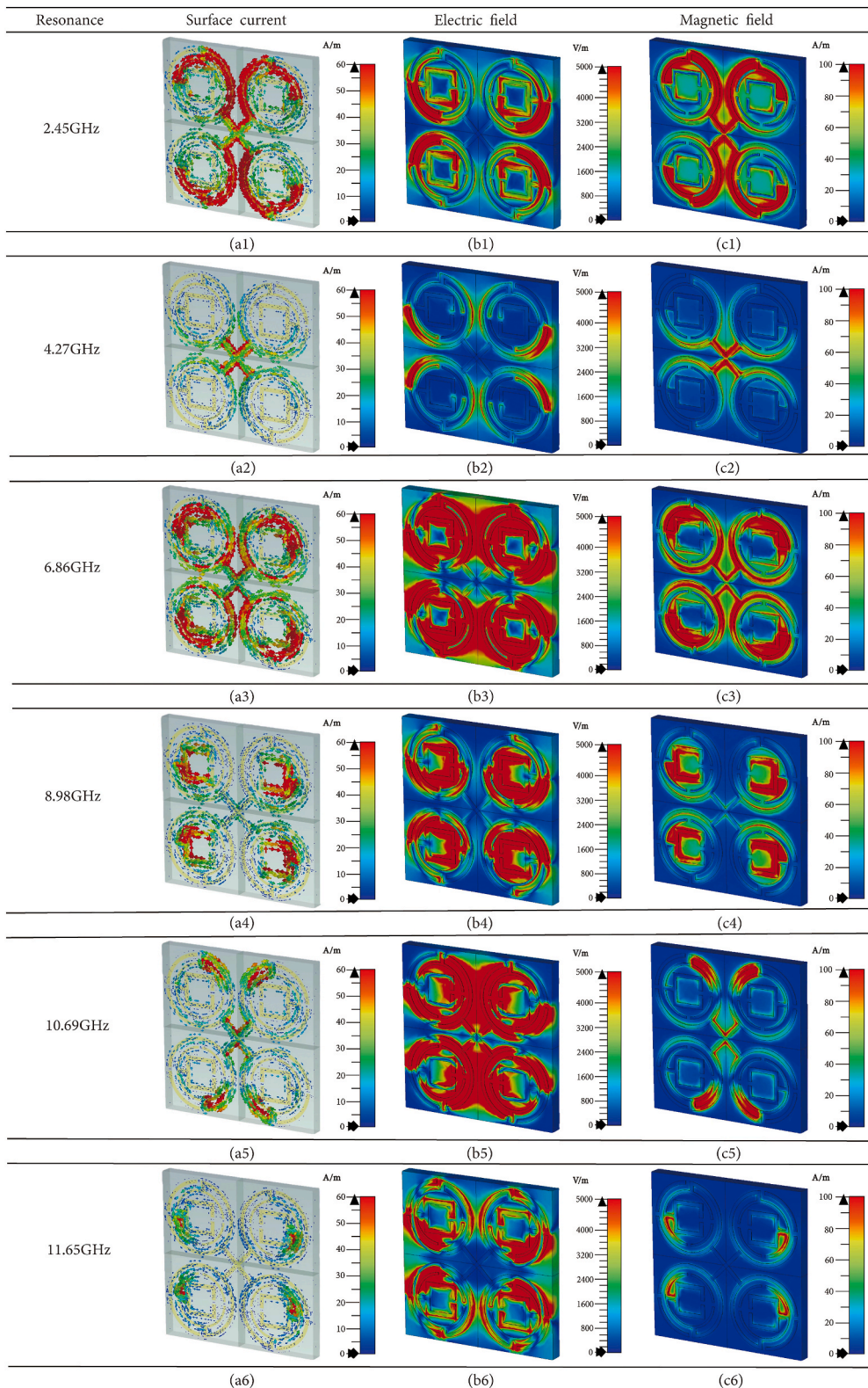| Resonance	Surface current	Electric field	Magnetic field
2.45GHz	(a1)	(b1)	(c1)
4.27GHz	(a2)	(b2)	(c2)
6.86GHz	(a3)	(b3)	(c3)
8.98GHz	(a4)	(b4)	(c4)
10.69GHz	(a5)	(b5)	(c5)
11.65GHz	(a6)	(b6)	(c6)

Fig. 10. Surface current, electric field and magnetic field distribution (Left to right) at different resonant frequencies.

due to the configuration of circular split ring resonator and the design of the central cross structure, the currents of each subunit can also generate a strong composite magnetic field. This also can be supported by the corresponding magnetic field distribution in Fig. 10 (c1). On the other hand, the electric field shown in Fig. 10(b1) is predominantly distributed on both sides of the x-axis, away from the y-axis. In contrast, at the resonance point of 4.27 GHz, the surface current shown in Fig. 10(a2) is mainly concentrated at the cross-connections, and the currents in the outermost rings of each unit on both sides of the x-axis flow in the same direction. Therefore, the formed magnetic field should primarily concentrate at the cross-connections and on both sides of the x-axis which is shown in Fig. 10 (c2), with relatively stronger magnetic field in the cross-sectional area. In Fig. 10(b2) the electric field is mainly distributed near both sides of the y-axis and the left and right edges of the overall structure, with slightly stronger electric field intensity at the edges. At the resonance frequency of 6.86 GHz, the surface current shown in Fig. 10(a3) is mainly concentrated in the middle resonant loops, located near the four corners of the entire structure. Another portion of the current is concentrated on both sides of the center point, connected by the cross-section. The electric field is distributed almost within each resonant loop, but relatively weaker in the central cross-section in Fig. 10(b3). Near the resonance point of 8.98 GHz, the distribution of surface current shown in Fig. 10(a4) mainly concentrates near the inner square resonant loops, while the electric and magnetic field intensities are relatively weaker at the center cross-section in Fig. 10(c4). At the frequency point of 10.69 GHz, the strength of the surface current shown in Fig. 10(a5) is relatively stronger at the central cross-section, the upper and lower regions near the y-axis. Conversely, the electric field intensity is almost uniformly distributed throughout the entire structure except for the four corner areas shown in Fig. 10(b5). At the resonance frequency of 11.65 GHz, the surface current in Fig. 10(a6) predominantly distributes on the left and right sides of the system, near the x-axis, with a relatively small area. The electric field distribution in Fig. 10(b6) primarily concentrates in the central region, at the locations of the inner and middle resonant loops.

4. Measurement results and discussion

The simulation results were further verified by measuring fabricated MM samples using performance network analyzer (PNA) shown in Fig. 11 (right). Since each adapter operates in a specific frequency range, 5 different waveguide adapter groups are required to achieve measurements in the range from 2 GHz to 12GHz. They are 1.72GHz–2.61 GHz, 2.6–3.95 GHz, 3.94–5.99 GHz, 5.37–8.17 GHz and 8.2–12.5 GHz.

During the measurement, the VNA is cabled to two waveguide ports, as shown in Fig. 11 (left), which serve as transmit and receive ports, while the MM structure is placed between them. The measurement results present the six resonant frequencies of S21 at 2.48 GHz, 4.28 GHz, 6.65 GHz, 9.13 GHz, 10.48 GHz, and 11.42 GHz shown in Fig. 12. The snapshots of S21 measurement are displayed in Fig. S2 in the Supplementary Information. Comparing with the simulation results obtained in CST, the resonance frequency deviations were 1.2 %, 0.2 %, 3 %, 1.5 %, 1.9 % and 2 %, respectively. The actual measurement bandwidths at each resonant peak are 0.36 GHz, 0.51 GHz, 0.16 GHz, 0.38 GHz, 0.21 GHz, and 0.74 GHz. Compared to the theoretical bandwidth, the measured bandwidth at 4.27 GHz is small, and the bandwidth at the other five resonances is higher. The main errors between theoretical simulations and practical measurements are contributed by the precision of fabricating device, and the network matching between the various converters during actual measurements. The accumulation of these errors can lead to slight deviations at each resonant frequency, as well as small frequency fluctuations. Neglecting these errors, the experimental measurement results are in perfect agreement with the theoretical simulation, exhibiting excellent response in the corresponding frequency bands.

5. Comparative analysis

Comparisons were made between the proposed MM structure and the reported work previously, with the physical dimensions, resonant frequency, bandwidth, and Effective Medium Ratio (EMR) of the Metamaterial (MM) being the main parameters. The formula for calculating the EMR is as follows:

$$EMR = \lambda/L \tag{14}$$

where λ is the wavelength calculated at the lowest resonant frequency and L is the highest dimensional value of the MM structure. The articles in Table 3 are arranged in chronological order of publication. From the table, it can be observed that Refs [32,38,41,42,43,46, 48]. exhibit higher EMR values, indicating their compactness in design. However, compared to our proposed design, they have fewer resonance modes resulting in a narrower operating frequency range. Refs [20,44,45,47]. have smaller physical dimensions for their MM structures compared to our proposed dimensions, but they have lower EMR values. Compared to other existing techniques in Table 3, the proposed MM demonstrates superiority in terms of physical dimensions, resonance modes, and bandwidth coverage. In addition, the structure proposed in this article exhibits high frequency selectivity in the S, C, and X bands.

6. Conclusion

In this study, we present a polarization-insensitive and double-negative symmetric metamaterial resonator with six resonance frequencies covering S, C, and X bands. The resonances occur at 2.45 GHz, 4.27 GHz, 6.86 GHz, 8.98 GHz, 10.69 GHz, and 11.65 GHz, respectively, with S21 values of −15dB or below. The resonator-based MM is composed of four sub meta-atoms, with a total size of 20 × 20 × 1.575 mm excluding the 0.035 mm copper thickness. The symmetry combination of mirror and center leads to the elimination of coupling effects between meta-atoms, minimizing resonance deviation between the meta-atom and its arrays. Additionally, the
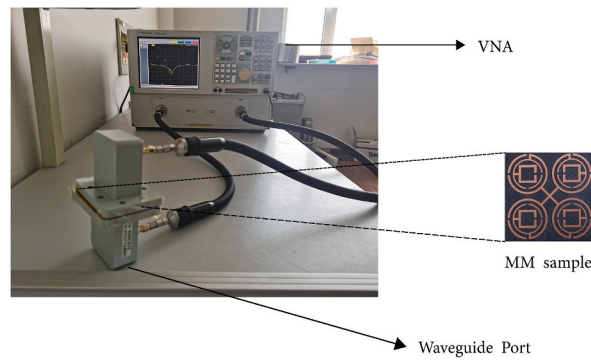
Fig. 11. Experimental setup using PNA and waveguide port(left), Fabricated prototype of 2 × 2 array of proposed MM (right).
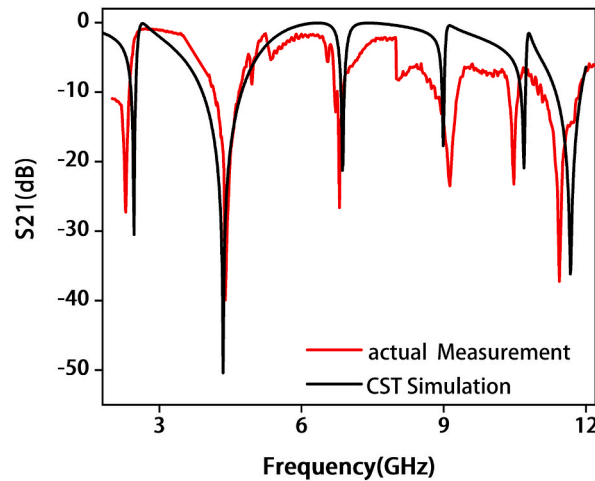

Fig. 12. Comparative analysis of the experimental transmission coefficient (S21) of the proposed unit cell with theoretical simulations conducted in CST.

Table 3
Performance analysis of the proposed metamaterial (MTM) against relevant.

References	Years	Dimension physical(mm × mm)	Resonance frequency (GHz)	Frequency band	EMR
[40]	2018	20 × 20	13.78, 15.30	X and Ku	1.3
[45]	2018	9 × 8.8	9.65, 12.60	X and Ku	3.45
[32]	2019	9 × 9	4.15, 10.84, 14.93	C, X and Ku	8.03
[41]	2019	5.5 × 5.5	7.50	C	8
[42]	2020	10 × 10	3.57, 11.60	S and X	8.4
[43]	2020	8 × 8	2.61, 6.32, 9.29	S, C and X	14.37
[44]	2020	10 × 10	6.53, 10.63, 13.35	C, X and Ku	4.5
[20]	2021	8 × 8	8.67, 13.84	X and Ku	4.3
[38]	2022	20 × 20	1.98, 3.67, 4.74, 8.38, 10.80	L, S, C and X	7.57
[47]	2022	10 × 10	6.31, 7.79, 9.98, 10.82, 11.86, 13.36, 15.5	C, X and Ku	4.8
[46]	2023	8 × 8	2.40, 4.50,7.24	S and C	15.61
[48]	2023	14.5 × 14.5	2.88, 4.78, 10.9	S, C and X	7.19
Proposed	2023	20 × 20	2.45, 4.27, 6.86, 8.98, 10.69, 11.65	S, C and X	6.12

proposed MM resonator exhibits unique electromagnetic properties such as negative permittivity, negative permeability, and moderate EMR. Furthermore, we demonstrated a tunable sandwiched metamaterial in which the resonance frequencies can be swept over a frequency span of 1 GHz by controlling the gap opening of the top dielectric layer. The experimental measurements agreed perfectly with numerical simulations. Due to its exceptional properties, our proposed MM design holds great potential for applications in microwave communications, satellites, radars, and beyond. We also investigated a feasible way to achieve the tunability of MM devices, which may find use in frequency-selective sensing and stealth applications. Notably, this technique can be extended to terahertz frequencies.

Data availability statement

The data that support the findings of this study are available from the corresponding author upon reasonable request.

CRediT authorship contribution statement

Zhonghang Ji: Writing – original draft, Validation, Software, Methodology, Investigation, Funding acquisition, Data curation, Conceptualization. **Wei Cao:** Validation, Software, Resources, Formal analysis, Data curation. **Mandi Gao:** Validation, Software, Resources, Investigation, Formal analysis, Data curation. **Yunqing Liu:** Validation, Supervision, Project administration, Methodology, Conceptualization. **Wei Chu:** Writing – review & editing, Writing – original draft, Supervision, Resources, Methodology, Data curation, Conceptualization. **Qiong Zhang:** Software, Resources, Funding acquisition, Formal analysis, Data curation.

Declaration of competing interest

The authors declare that they have no known competing financial interests or personal relationships that could have appeared to influence the work reported in this paper.

Acknowledgment

Appendix A. Supplementary data

Supplementary data to this article can be found online at https://doi.org/10.1016/j.heliyon.2023.e21731.

References

[1] M. Moniruzzaman, et al., Gap coupled symmetric split ring resonator based near zero index ENG metamaterial for gain improvement of monopole antenna, Sci. Rep. 12 (1) (May 2022) 7406, https://doi.org/10.1038/s41598-022-11029-7.

[2] T. Shabbir, et al., 16-Port non-planar MIMO antenna system with near-zero-index (NZI) metamaterial decoupling structure for 5G applications, IEEE Access 8 (2020) 157946–157958, https://doi.org/10.1109/ACCESS.2020.3020282.

[3] N. Hussain, M.-J. Jeong, A. Abbas, N. Kim, Metasurface-based single-layer wideband circularly polarized MIMO antenna for 5G millimeter-wave systems, IEEE Access 8 (2020) 130293–130304, https://doi.org/10.1109/ACCESS.2020.3009380.

[4] M. Moniruzzaman, M.T. Islam, G. Muhammad, M.S.J. Singh, M. Samsuzzaman, Quad band metamaterial absorber based on asymmetric circular split ring resonator for multiband microwave applications, Results Phys. 19 (October) (2020), 103467, https://doi.org/10.1016/j.rinp.2020.103467.

[5] L. Jiang, et al., Multi-band and high-sensitivity perfect absorber based on monolayer graphene metamaterial, Diam. Relat. Mater. 111 (Jan. 2021), 108227, https://doi.org/10.1016/j.diamond.2020.108227.

[6] Z. Luo, S. Ji, J. Zhao, H. Wu, H. Dai, A multiband metamaterial absorber for GHz and THz simultaneously, Results Phys. 30 (Nov. 2021), 104893, https://doi.org/10.1016/j.rinp.2021.104893.

[7] E. Razzicchia, I. Sotiriou, H. Cano-Garcia, E. Kallos, G. Palikaras, P. Kosmas, Feasibility study of enhancing microwave brain imaging using metamaterials, Sensors 19 (24) (Dec. 2019) 5472, https://doi.org/10.3390/s19245472.

[8] C. Lu, R. Yu, Q. Ma, K. Wang, J. Wang, D. Wu, GRIN metamaterial generalized Luneburg lens for ultra-long acoustic jet, Appl. Phys. Lett. 118 (14) (Apr. 2021), 144103, https://doi.org/10.1063/5.0044436.

[9] W. Xu, et al., Terahertz biosensing with a graphene-metamaterial heterostructure platform, Carbon N. Y. 141 (Jan. 2019) 247–252, https://doi.org/10.1016/j.carbon.2018.09.050.

[10] H. Chu, et al., A hybrid invisibility cloak based on integration of transparent metasurfaces and zero-index materials, Light Sci. Appl. 7 (1) (Aug. 2018) 50, https://doi.org/10.1038/s41377-018-0052-7.

[11] A.A. Musaed, S.S. Al-Bawri, M.T. Islam, A.J.A. Al-Gburi, M.J. Singh, Tunable compact metamaterial-based double-negative/near-zero index resonator for 6G terahertz wireless applications, Materials 15 (16) (Aug. 2022) 5608, https://doi.org/10.3390/ma15165608.

[12] N. Shlezinger, G.C. Alexandropoulos, M.F. Imani, Y.C. Eldar, D.R. Smith, Dynamic metasurface antennas for 6G extreme massive MIMO communications, IEEE Wireless Commun. 28 (2) (Apr. 2021) 106–113, https://doi.org/10.1109/MWC.001.2000267.

[13] L. Bariah, et al., A prospective look: key enabling technologies, applications and open research topics in 6G networks, IEEE Access 8 (2020) 174792–174820, https://doi.org/10.1109/ACCESS.2020.3019590.

[14] M. Bellal Hossain, M. Rashed Iqbal Faruque, A.S. Alshammari, M. Tariqul Islam, Wide bandwidth enriched symmetric hexagonal split ring resonator based triple band negative permittivity metamaterial for satellite and Wi-Fi applications, Results Phys. 37 (Jun. 2022), 105511, https://doi.org/10.1016/j.rinp.2022.105511.

[15] M.B. Hossain, M.R.I. Faruque, S. Abdullah, Modified combination of triple split ring resonator based triple band single negative metamaterial for satellite applications, IOP Conf. Ser. Earth Environ. Sci. 1167 (1) (May 2023), 012041, https://doi.org/10.1088/1755-1315/1167/1/012041.

[16] G. Geetharamani, T. Aathmanesan, Design of metamaterial antenna for 2.4 GHz WiFi applications, Wireless Pers. Commun. 113 (4) (Aug. 2020) 2289–2300, https://doi.org/10.1007/s11277-020-07324-z.

[17] A. Di Gaspare, et al., Tunable, grating-gated, graphene-on-polyimide terahertz modulators, Adv. Funct. Mater. 31 (10) (Mar. 2021), 2008039, https://doi.org/10.1002/adfm.202008039.

[18] Z. Li, H. Xia, Y. Zhao, W. Lei, C. Zhao, W. Xie, Polarization-insensitive and absorption-tunable ultra-broadband terahertz metamaterial absorbers based on multiple resonant rings, Results Phys. 39 (Aug. 2022), 105786, https://doi.org/10.1016/j.rinp.2022.105786.

[19] M.L. Hakim, T. Alam, A.F. Almutairi, M.F. Mansor, M.T. Islam, Polarization insensitivity characterization of dual-band perfect metamaterial absorber for K band sensing applications, Sci. Rep. 11 (1) (Sep. 2021), 17829, https://doi.org/10.1038/s41598-021-97395-0.

[20] T. Ramachandran, M.R.I. Faruque, M.T. Islam, A dual-band polarization-independent left-handed symmetrical metamaterial for communication system application, J. Mater. Res. Technol. 15 (Nov. 2021) 731–744, https://doi.org/10.1016/j.jmrt.2021.08.015.

[21] T. Yang, X. Liu, C. Wang, F. Wang, J. Zhou, High-efficiency cross-polarization conversion metamaterial using spiral split-ring resonators, AIP Adv. 10 (9) (2020), https://doi.org/10.1063/5.0017809.

[22] J.B. Pendry, A.J. Holden, W.J. Stewart, I. Youngs, Extremely low frequency plasmons in metallic mesostructures, Phys. Rev. Lett. 76 (25) (Jun. 1996) 4773–4776, https://doi.org/10.1103/PhysRevLett.76.4773.

[23] J.B. Pendry, A.J. Holden, D.J. Robbins, W.J. Stewart, Magnetism from conductors and enhanced nonlinear phenomena, IEEE Trans. Microw. Theor. Tech. 47 (11) (1999) 2075–2084, https://doi.org/10.1109/22.798002.

[24] D. Schurig, J.J. Mock, D.R. Smith, Electric-field-coupled resonators for negative permittivity metamaterials, Appl. Phys. Lett. 88 (4) (Jan. 2006), 041109, https://doi.org/10.1063/1.2166681.

[25] H.-T. Chen, et al., Complementary planar terahertz metamaterials, Opt Express 15 (3) (2007) 1084, https://doi.org/10.1364/oe.15.001084.

[26] W.J. Padilla, M.T. Aronsson, C. Highstrete, M. Lee, A.J. Taylor, R.D. Averitt, Electrically resonant terahertz metamaterials: theoretical and experimental investigations, Phys. Rev. B Condens. Matter 75 (4) (2007) 1–4, https://doi.org/10.1103/PhysRevB.75.041102.

[27] S.S. Al-Bawri, M.T. Islam, M.S. Islam, M.J. Singh, H. Alsaif, Massive metamaterial system-loaded MIMO antenna array for 5G base stations, Sci. Rep. 12 (1) (2022), https://doi.org/10.1038/s41598-022-18329-y.

[28] M. Moniruzzaman, M.T. Islam, I. Hossain, M.S. Soliman, M. Samsuzzaman, S.H.A. Almalki, Symmetric resonator based tunable epsilon negative near zero index metamaterial with high effective medium ratio for multiband wireless applications, Sci. Rep. 11 (1) (Nov. 2021), 21842, https://doi.org/10.1038/s41598-021-01266-7.

[29] J. Chen, X. Lian, M. Zhao, C. Xie, Multimode fano resonances sensing based on a non-through MIM waveguide with a square split-ring resonance cavity, Biosensors 12 (5) (2022) 1–14, https://doi.org/10.3390/bios12050306.

[30] T. Xiang, T. Lei, J. Wu, J. Wang, H. Yang, Dual-Fano resonances based on all-dielectric toroidal metamaterial, APEX 15 (3) (2022) 0–5, https://doi.org/10.35848/1882-0786/ac4e27.

[31] M.T. Islam, M. Moniruzzaman, T. Alam, M. Samsuzzaman, Q.A. Razouqi, A.F. Almutairi, Realization of frequency hopping characteristics of an epsilon negative metamaterial with high effective medium ratio for multiband microwave applications, Sci. Rep. 11 (1) (2021) 1–23, https://doi.org/10.1038/s41598-021-96228-4.

[32] M. Moniruzzaman, M.T. Islam, M. Tarikul Islam, M.E.H. Chowdhury, H. Rmili, M. Samsuzzaman, Cross coupled interlinked split ring resonator based epsilon negative metamaterial with high effective medium ratio for multiband satellite and radar communications, Results Phys. 18 (July) (2020), 103296, https://doi.org/10.1016/j.rinp.2020.103296.

[33] M.R. Islam, M. Samsuzzaman, N. Misran, G.K. Beng, M.T. Islam, A tri-band left-handed meta-atom enabled designed with high effective medium ratio for microwave based applications, Results Phys. 17 (February) (2020), 103032, https://doi.org/10.1016/j.rinp.2020.103032.

[34] S. Hannan, M.T. Islam, M.R.I. Faruque, H. Rmili, Polarization-independent perfect metamaterial absorber for C, X and, Ku band applications, J. Mater. Res. Technol. 15 (2021) 3722–3732, https://doi.org/10.1016/j.jmrt.2021.10.007.

[35] Y. Wen, T. Xu, Y.S. Lin, Design of electrostatically tunable terahertz metamaterial with polarization-dependent sensing characteristic, Results Phys. 29 (2021), 104798, https://doi.org/10.1016/j.rinp.2021.104798.

[36] P. Zhang, et al., Ultra-broadband tunable terahertz metamaterial absorber based on double-layer vanadium dioxide square ring arrays, Micromachines 13 (5) (Apr. 2022) 669, https://doi.org/10.3390/mi13050669.

[37] G. Yang, et al., Tunable broadband terahertz metamaterial absorber based on vanadium dioxide, AIP Adv. 12 (4) (Apr. 2022), 045219, https://doi.org/10.1063/5.0082295.

[38] M. Moniruzzaman, et al., Electromagnetic characterization of mirror symmetric resonator based metamaterial and frequency tuning: a dielectric based multilayer approach, Sci. Rep. 12 (1) (Jul. 2022), 12497, https://doi.org/10.1038/s41598-022-16443-5.

[39] X. Chen, T.M. Grzegorczyk, B.I. Wu, J. Pacheco, J.A. Kong, Robust method to retrieve the constitutive effective parameters of metamaterials, Phys. Rev. E 70 (1) (2004) 7, https://doi.org/10.1103/PhysRevE.70.016608.

[40] A. Hoque, M.T. Islam, A.F. Almutairi, T. Alam, M.J. Singh, N. Amin, A polarization independent quasi-TEM metamaterial absorber for X and ku band sensing applications, Sensors 18 (12) (2018), https://doi.org/10.3390/s18124209.

[41] A.F. Almutairi, M.S. Islam, M. Samsuzzaman, M.T. Islam, N. Misran, M.T. Islam, A complementary split ring resonator based metamaterial with effective medium ratio for C-band microwave applications, Results Phys. 15 (Dec) (2019), https://doi.org/10.1016/j.rinp.2019.102675.

[42] M. Shahidul Islam, M. Samsuzzaman, G.K. Beng, N. Amin, M.T. Islam, A gap coupled hexagonal split ring resonator based metamaterial for S-band and X-band microwave applications, IEEE Access 8 (2020) 68239–68253, https://doi.org/10.1109/ACCESS.2020.2985845.

[43] M. Rashedul Islam, et al., Square enclosed circle split ring resonator enabled epsilon negative (ENG) near zero index (NZI) metamaterial for gain enhancement of multiband satellite and radar antenna applications, Results Phys. 19 (Dec) (2020), https://doi.org/10.1016/j.rinp.2020.103556.

[44] M. Shahidul Islam, M.T. Islam, N. Mohd Sahar, H. Rmili, N. Amin, M.E.H. Chowdhury, A mutual coupled concentric crossed-Line split ring resonator (CCSRR) based epsilon negative (ENG) metamaterial for Tri-band microwave applications, Results Phys. 18 (Sep. 2020), https://doi.org/10.1016/j.rinp.2020.103292.

[45] T.M. Hossain, M.F. Jamlos, M.A. Jamlos, P.J. Soh, M.I. Islam, R. Khan, Modified H-shaped DNG metamaterial for multiband microwave application, Appl. Phys. Mater. Sci. Process 124 (2) (Feb. 2018), https://doi.org/10.1007/s00339-018-1593-6.

[46] A. Hussain, et al., A double negative (DNG) metamaterial based on parallel double-E square split resonators for multi-band applications: simulation and experiment, Results Phys. 46 (Mar. 2023), https://doi.org/10.1016/j.rinp.2023.106302.

[47] B. Ajewole, P. Kumar, T. Afullo, I-shaped metamaterial using SRR for multi-band wireless communication, Crystals 12 (4) (2022), https://doi.org/10.3390/cryst12040559.

[48] S. Hossen, A. Alqahtani, I. Hossain, M.T. Islam, M. Moniruzzaman, M. Samsuzzaman, Gap coupled symmetric square split ring high EMR resonator-based metamaterial for S-, C-, and X-bands wireless applications: simulation and experiment, Opt. Mater. 145 (September) (2023), 114389, https://doi.org/10.1016/j.optmat.2023.114389.